



# Nanoconfined catalytic membranes assembled by cobalt-functionalized graphitic carbon nitride nanosheets for rapid degradation of pollutants

Wei Zhang <sup>a,b,c,1</sup>, Shaoze Zhang <sup>d,1</sup>, Chenchen Meng <sup>a</sup>, Zhenghua Zhang <sup>a,b,c,\*</sup>

<sup>a</sup> Institute of Environment and Ecology, Tsinghua Shenzhen International Graduate School, Tsinghua University, Shenzhen 518055, Guangdong, China

<sup>b</sup> Guangdong Provincial Engineering Research Center for Urban Water Recycling and Environmental Safety, Tsinghua-Shenzhen International Graduate School, Tsinghua University, Shenzhen 518055, Guangdong, China

<sup>c</sup> School of Environment, Tsinghua University, Beijing 100084, China

<sup>d</sup> National Engineering Research Center for Vacuum Metallurgy, Engineering Laboratory for Advanced Battery and Materials of Yunnan Province, Kunming University of Science and Technology, Kunming 650093, Yunnan Province, China



## ARTICLE INFO

### Keywords:

Nanoconfinement catalysis  
Catalytic membrane  
Graphitic carbon nitride  
Cobalt(II) oxide  
Peroxymonosulfate

## ABSTRACT

Sulfate radical-based advanced oxidation processes (SR-AOPs) constitute an efficient method for the effective removal of organic pollutants in water bodies. A novel cobalt-functionalized graphitic carbon nitride ( $\text{Co@g-C}_3\text{N}_4$ ) membrane was designed and prepared for the first time to activate peroxymonosulfate (PMS) for pollutant degradation. The prepared  $\text{Co@g-C}_3\text{N}_4$  membrane demonstrated a long-term stability over 100 h continuous operation at a flux of  $113.2 \text{ L}\cdot\text{m}^{-2}\cdot\text{h}^{-1}$  and a retention time of 33 ms for 100 % removal of ranitidine (5 mg/L) as the target pollutant with the first-order rate constant 4–6 orders of magnitude higher than that in previously reported AOP systems. Singlet oxygen significantly contributed to the degradation of diverse pollutants within the numberless nanoconfined spaces of membrane. Oxygen vacancies in  $\text{Co@g-C}_3\text{N}_4$  can effectively promote the redox cycle of  $\equiv\text{Co(II)}/\equiv\text{Co(III)}$  to maintain the catalytically active center. The developed membrane herein combining membrane filtration and AOP would provide a novel strategy for water and wastewater treatment.

## 1. Introduction

With the development of social economy and industry, many synthetic organic products (such as pharmaceutical and personal care products (PPCPs) and dyes) are discharged into the water environment, causing serious environmental pollution as contaminants and aggravating the problems of limited freshwater resources [1,2]. These refractory organic contaminants (ROCs) generally possess stable structures and are difficult to remove from water by traditional wastewater treatment methods. Therefore, it is necessary to develop effective methods for ROC degradation in water. Advanced oxidation processes (AOPs) have been widely used to degrade ROCs in water [3,4]. Nowadays, sulfate radical ( $\text{SO}_4^{\cdot-}$ )-based AOPs (SR-AOPs) have attracted extensive attention due to the unique advantages of  $\text{SO}_4^{\cdot-}$  [5], including the stronger oxidation ability ( $E^\circ = 2.6\text{--}3.1 \text{ V}$ ) compared to the hydroxyl radical ( $\cdot\text{OH}$ ) ( $E^\circ = 1.9\text{--}2.7 \text{ V}$ ) [6].

Peroxymonosulfate (PMS) is a suitable, strong oxidant to produce

$\text{SO}_4^{\cdot-}$ . However, its direct reaction with contaminants is too slow so that activation is needed [7]. Among the various activation systems, cobalt (II) oxide (CoO) has been proved to be an effective catalyst for PMS activation [8,9]. However, the secondary pollution caused by cobalt ion leaching is a serious challenge [10,11]. In addition, the easy aggregation of CoO nanoparticles leads to the deactivation of CoO within a short reaction time [12]. Immobilizing CoO on specific materials is a feasible solution to reduce the leaching of cobalt ions, which can increase catalyst stability and improve their reusability [6,9,13].

Very recently, graphitic carbon nitride ( $\text{g-C}_3\text{N}_4$ ) has attracted great interest in the application field of wastewater treatment due to its excellent electronic properties, outstanding chemical and thermal stability, simple synthesis, and environmental friendliness [14,15].  $\text{g-C}_3\text{N}_4$  sheets form bulk  $\text{g-C}_3\text{N}_4$  through weak van der Waals force interaction [16]. However, bulk  $\text{g-C}_3\text{N}_4$  still encounters some limitations, such as poor electrical conductivity and low specific surface area [12]. Some studies have confirmed the better performance of  $\text{g-C}_3\text{N}_4$  nanosheets

\* Corresponding author at: Institute of Environment and Ecology, Tsinghua Shenzhen International Graduate School, Tsinghua University, Shenzhen 518055, Guangdong, China.

E-mail address: [zhenghua.zhang@sz.tsinghua.edu.cn](mailto:zhenghua.zhang@sz.tsinghua.edu.cn) (Z. Zhang).

<sup>1</sup> Co-first authors

(g-C<sub>3</sub>N<sub>4</sub> NS) exfoliated from bulk g-C<sub>3</sub>N<sub>4</sub> [17,18]. Several exfoliation approaches, including chemical exfoliation, ultrasonic exfoliation, and thermal exfoliation, have been applied to produce g-C<sub>3</sub>N<sub>4</sub> NS [19–21]. g-C<sub>3</sub>N<sub>4</sub> NS have large specific surface areas and flexible two-dimensional (2D) structures, thus CoO can be anchored on the surface of g-C<sub>3</sub>N<sub>4</sub> NS to effectively prevent its aggregation [22,23].

Explorations on CoO-modified g-C<sub>3</sub>N<sub>4</sub> have focused on the photocatalytic degradation of organic pollutants in wastewater [12,22]. Only a few studies have investigated the performance of cobalt-modified g-C<sub>3</sub>N<sub>4</sub> in the field of PMS activation. Sodium borohydride-treated cobalt-doped g-C<sub>3</sub>N<sub>4</sub> can effectively contact PMS and activate it through electrostatic attraction [24]. Cobalt(II)- and cobalt(III)-doped g-C<sub>3</sub>N<sub>4</sub> can effectively activate PMS for monochlorophenol degradation [25]. However, in these studies, the valence state of cobalt is not regulated in cobalt-doped g-C<sub>3</sub>N<sub>4</sub>, which may affect PMS activation. The catalytic stability of cobalt-doped g-C<sub>3</sub>N<sub>4</sub> still needs to be further improved. The mechanism of electron transfer during PMS activation is also unclear.

Electronic structure and mass transfer can be changed due to the nanoconfinement effect when the reaction system is limited in the available nanoscale space. Nanoconfined space can enrich reactants and prolong the residence time of reactants on the catalyst surface, resulting in improved catalytic performance [26]. It is worth noting that the traditional catalytic suspension system has low mass transfer efficiency [27], and it is necessary to change the operation mode of the catalytic system to improve mass transfer efficiency. Combining SR-AOPs with membrane filtration to prepare catalytic membranes with self-cleaning ability is a promising approach to water treatment. The mass transfer distance is shortened in nanoconfined spaces of membrane, so that generated reactive oxygen species (ROS) can quickly contact and degrade target pollutants. Furthermore, the limitations including severe agglomeration and low recovery of nanomaterials in conventional batch-mode suspension systems would be well addressed by anchoring nanomaterials onto 2D NS and then assembling into membranes. Therefore, the construction of catalytic membranes with nanoconfined structures is an effective means to achieve advanced water and wastewater treatment.

Recently, membrane-based nanoconfined catalysis has been reported for water treatment. The currently reported development strategies of membrane-based nanoconfined catalysis include (1) layered assembly of 2D nanosheets (2D molybdenum disulfide NS [27], 2D metal oxide NS [31]), (2) loading nanocatalysts on commercial membrane [28] and (3) layered assembly of 2D nanosheets functionalized with nanocatalysts [29]. The difficulty in the development of membrane-based nanoconfined catalysis is to overcome the permeability-degradation efficiency trade-off by maintaining its catalytic stability under a relatively high water flux (e.g. >100 L·m<sup>-2</sup>·h<sup>-1</sup>).

With the above factors, we envisage coupling g-C<sub>3</sub>N<sub>4</sub> NS with CoO nanoparticles to form Co@g-C<sub>3</sub>N<sub>4</sub> membranes with stable and efficient catalytic ability. In this work, Co@g-C<sub>3</sub>N<sub>4</sub> nanosheets (Co@g-C<sub>3</sub>N<sub>4</sub> NS) were prepared by simple thermal annealing in nitrogen atmosphere [15]. Then, the Co@g-C<sub>3</sub>N<sub>4</sub> membranes were prepared for ROC degradation through a vacuum-assisted filtration approach using Co@g-C<sub>3</sub>N<sub>4</sub> NS. The Co@g-C<sub>3</sub>N<sub>4</sub> membranes and their morphology, chemical composition, and catalytic degradation properties were studied in detail. The pollutant degradation and PMS activation mechanisms were systematically elucidated by theoretical calculations (density functional theory calculations) and state-of-the-art characterizations.

## 2. Experimental section

### 2.1. Materials and reagents

The used reagents and materials are listed in detail in the supporting information (Text S1).

### 2.2. Preparation of Co@g-C<sub>3</sub>N<sub>4</sub> nanosheets

g-C<sub>3</sub>N<sub>4</sub> was synthesized from urea in a thermal oxidation process [22,23]. As shown in Fig. 1, 20 g urea was placed in a covered porcelain crucible and calcined at 550 °C for 2 h in air with a heating rate of 2 °C/min. After cooling to room temperature, bulk g-C<sub>3</sub>N<sub>4</sub> was obtained as the product. Then, to synthesize g-C<sub>3</sub>N<sub>4</sub> NS, bulk g-C<sub>3</sub>N<sub>4</sub> powder was calcined in a muffle furnace at 500 °C for another 2 h using a heating rate of 5 °C/min and then cooled naturally to room temperature.

Amounts of 500 mg g-C<sub>3</sub>N<sub>4</sub> NS and 100 mg cobalt acetate were added to 50 mL ethanol (EtOH) and sonicated for 15 min before stirring at room temperature for 24 h until the solvent was completely evaporated. Subsequently, the remaining mixture was dried in an oven at 60 °C for 1 h. The dried sample was calcined at 400 °C for 2 h in a tubular furnace under nitrogen atmosphere at a heating rate of 5 °C/min to obtain Co@g-C<sub>3</sub>N<sub>4</sub> NS after cooling to room temperature.

### 2.3. Preparation of Co@g-C<sub>3</sub>N<sub>4</sub> membranes

The obtained Co@g-C<sub>3</sub>N<sub>4</sub> NS (400 µg, 600 µg, 1 mg, 3 mg, 6 mg, 9 mg, 18 mg) were dispersed in 200 mL Milli-Q water and ultrasonicated for 30 min. Then, the Co@g-C<sub>3</sub>N<sub>4</sub> membranes were prepared by passing the 200 mL uniformly dispersed suspension through a cellulose acetate membrane by applying continuous vacuum filtration (Fig. 1). After filtration, the membrane was taken out, kept in air for 1 h, and then placed in a drying oven for 1 h at 40 °C.

### 2.4. Characterizations

The microstructure and morphology of Co@g-C<sub>3</sub>N<sub>4</sub> NS were assessed by transmission electron microscopy (TEM; FEI Talos F200S, Thermo Fisher Scientific, USA) and scanning electron microscopy (SEM) coupled with energy dispersive X-ray spectroscopy (EDX) (SU8010, Hitachi, Japan). The morphology and thickness of Co@g-C<sub>3</sub>N<sub>4</sub> NS were identified by atomic force microscopy (AFM) (Cyper ES, Oxford Instruments, UK). The crystal structures of the catalysts were examined by X-ray diffraction (XRD; Ultima IV, Rigaku Corp., Japan). The chemical bonds contained in the samples were observed by Fourier transform infrared (FTIR) spectroscopy (Nicolet iS20, Thermo Fisher Scientific, USA). The specific bonding and chemical states of elements in g-C<sub>3</sub>N<sub>4</sub> NS and Co@g-C<sub>3</sub>N<sub>4</sub> NS were determined by X-ray photoelectron spectroscopy (XPS; PHI 5000 VersaProbe II, PHI, Japan). The active species produced in the catalytic process were detected by electron paramagnetic resonance (EPR) spectroscopy (MS-5000, Bruker, Germany). The specific surface area and the pore size distribution of Co@g-C<sub>3</sub>N<sub>4</sub> NS were determined by nitrogen adsorption-desorption isotherms using the Brunauer-Emmett-Teller (BET) equation (ASAP 2460, Micromeritics, USA). Inductively coupled plasma mass spectrometry (ICP-MS, ICP-MS 7700, Agilent, USA) was used to quantify leached cobalt. Total organic carbon (TOC) analyzer (TOC-VCPH, Shimadzu, Japan) was used to measure the mineralization efficiency of pollutants. Liquid chromatography/tandem mass spectrometry (LC-MS, 1290UPLC-6550QTOF, Agilent, USA) was adopted to analyze degradation products (Table S1). Density functional theory (DFT) calculations were performed using the Vienna Ab initio Simulation Package (VASP) software (Text S2).

### 2.5. Catalytic activity of the Co@g-C<sub>3</sub>N<sub>4</sub> membrane

The catalytic degradation of ROCs was conducted using a vacuum-assisted filtration device with an effective filtration surface area of 1.766 cm<sup>2</sup> at 25 °C. The flux  $J$  (L·m<sup>-2</sup>·h<sup>-1</sup>) through the Co@g-C<sub>3</sub>N<sub>4</sub> membrane was calculated using Eq. (1):

$$J = \frac{V_l}{A_m \times T} \quad (1)$$

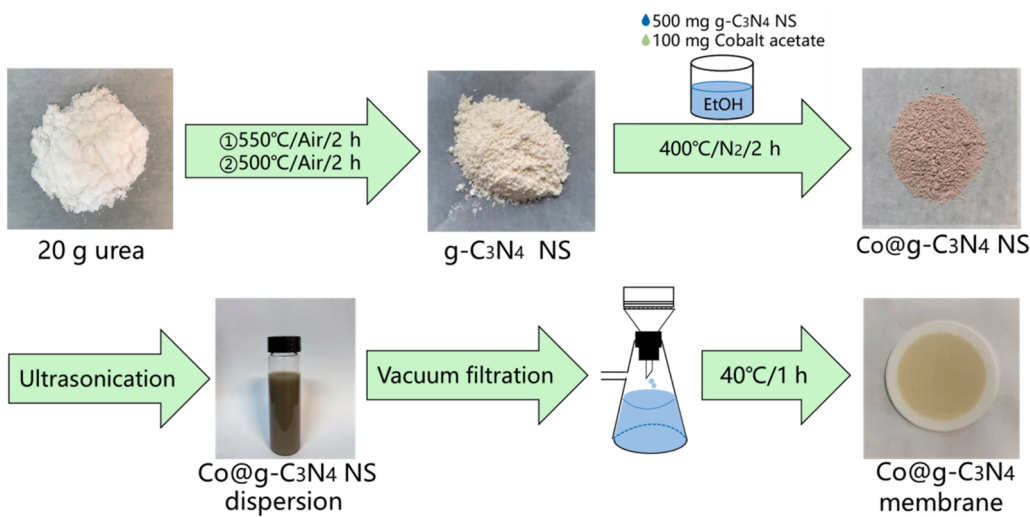


Fig. 1. Schematic of Co@g-C<sub>3</sub>N<sub>4</sub> NS synthesis and vacuum-assisted fabrication of Co@g-C<sub>3</sub>N<sub>4</sub> membranes.

where  $J$  is the membrane water flux;  $V_l$  (L) is the membrane-permeated solution volume;  $A_m$  (m<sup>2</sup>) is the effective membrane filtration surface area;  $T$  (h) represents the filtration time.

The removal efficiency of ROCs,  $R$  (%), was calculated using Eq. (2):

$$R = \frac{C_0 - C_p}{C_0} \times 100\% \quad (2)$$

where  $C_0$  (mg/L) represents the ROC concentration in the feed solution, and  $C_p$  (mg/L) indicates the ROC concentration in the filtrate.

## 2.6. Quenching experiments

To determine the ROS produced in the catalytic process, *tert*-butanol (TBA, 180 mM) and methanol (MeOH, 360 mM) were used to quench

•OH, while methanol was regarded as a quencher for both •OH and SO<sub>4</sub><sup>2-</sup>. Singlet oxygen (<sup>1</sup>O<sub>2</sub>) was quenched using 2,2,6,6-tetramethylpiperidine (TEMP, 5 mM). Before filtering an aqueous solution containing ranitidine (5 mg/L) and PMS (0.16 mM) through the Co@g-C<sub>3</sub>N<sub>4</sub> membrane, each of the above scavengers was added separately to the solution.

## 3. Results and discussion

### 3.1. Characterization of Co@g-C<sub>3</sub>N<sub>4</sub> nanosheets

The morphology of Co@g-C<sub>3</sub>N<sub>4</sub> NS was investigated by SEM and TEM. TEM images were recorded to show an overview of Co@g-C<sub>3</sub>N<sub>4</sub> NS. In Fig. 2a, the bulk g-C<sub>3</sub>N<sub>4</sub> was exfoliated into planar sheets after secondary calcination. Fig. 2b shows the SEM images of Co@g-C<sub>3</sub>N<sub>4</sub> NS,

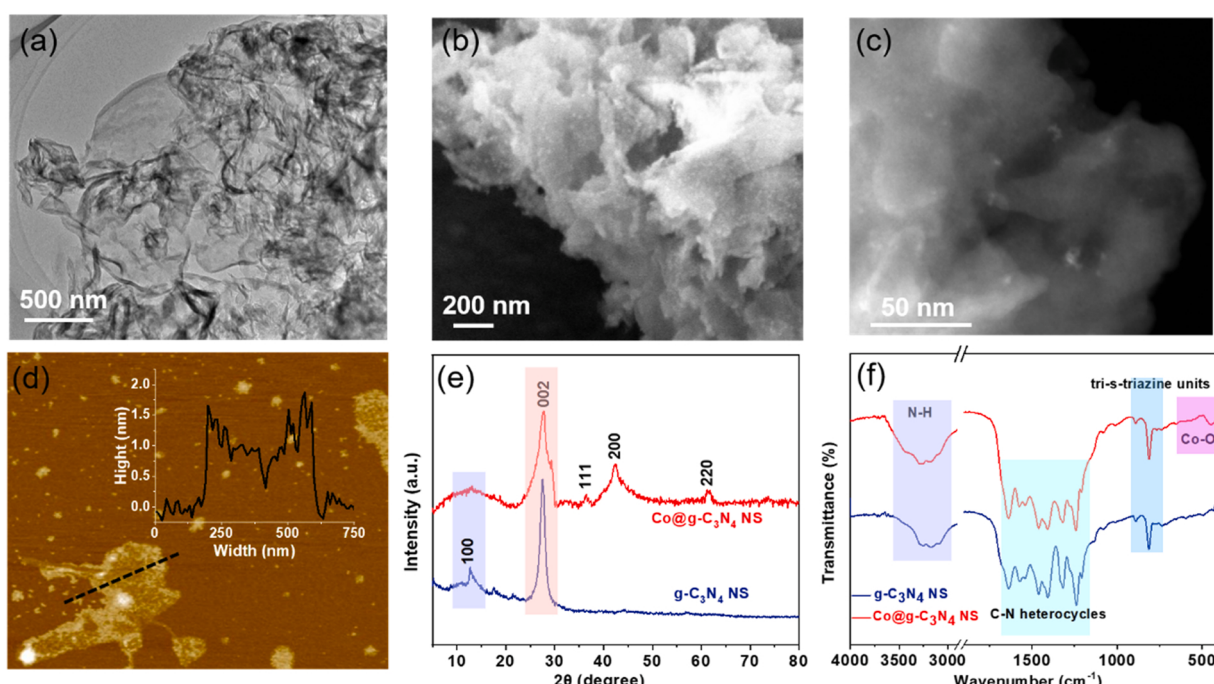


Fig. 2. (a) TEM image of Co@g-C<sub>3</sub>N<sub>4</sub> NS; (b) SEM image of Co@g-C<sub>3</sub>N<sub>4</sub> NS; (c) High-angle annular dark-field scanning transmission electron microscopy (HAADF-STEM) image of Co@g-C<sub>3</sub>N<sub>4</sub> NS; (d) AFM image and the height profile of the section along the black dashed line; (e) XRD patterns of g-C<sub>3</sub>N<sub>4</sub> NS and Co@g-C<sub>3</sub>N<sub>4</sub> NS; (f) FTIR spectra of g-C<sub>3</sub>N<sub>4</sub> NS and Co@g-C<sub>3</sub>N<sub>4</sub> NS.

which assumed a wrinkled-layer structure formed by the stacking of multiple irregular nanosheets. Furthermore, CoO nanoparticles were uniformly anchored on the surface of g-C<sub>3</sub>N<sub>4</sub> NS (Fig. 2c). The average particle size of CoO nanocatalysts anchored on the g-C<sub>3</sub>N<sub>4</sub> substrate was 11.1 nm (Fig. S1). The small particle size was because the adsorption of cobalt ions on the surface of g-C<sub>3</sub>N<sub>4</sub> limited the growth of CoO nanocatalysts [12,22]. AFM was performed to evaluate the nanosheet thickness of Co@g-C<sub>3</sub>N<sub>4</sub> NS, which was found to be between 1.5 and 2.0 nm (Fig. 2d).

The crystal structures of g-C<sub>3</sub>N<sub>4</sub> NS and Co@g-C<sub>3</sub>N<sub>4</sub> NS were determined by XRD. The characteristic structural features of g-C<sub>3</sub>N<sub>4</sub> were well preserved in Co@g-C<sub>3</sub>N<sub>4</sub> NS, indicating that the typical structure of g-C<sub>3</sub>N<sub>4</sub> did not change after surface modification with CoO nanoparticles. The g-C<sub>3</sub>N<sub>4</sub> NS and Co@g-C<sub>3</sub>N<sub>4</sub> NS showed obvious diffraction peaks at

$2\theta = 27.4^\circ$  and  $13.1^\circ$  in Fig. 2e, which could be ascribed to the (002) interlayer diffraction and (100) low-angle diffraction of g-C<sub>3</sub>N<sub>4</sub>, respectively [30,31]. It was noteworthy that the intensity of the Co@g-C<sub>3</sub>N<sub>4</sub> NS diffraction peaks was reduced compared to g-C<sub>3</sub>N<sub>4</sub> NS, which might be attributed to a decreased crystallinity of g-C<sub>3</sub>N<sub>4</sub> during nitrogen post-treatment [12]. In the XRD profile of Co@g-C<sub>3</sub>N<sub>4</sub> NS, the peaks at  $36.5^\circ$ ,  $42.4^\circ$ , and  $61.5^\circ$  could be attributed to the (111), (200), and (220) facets of cubic CoO, respectively, confirming the presence of CoO nanoparticles on the Co@g-C<sub>3</sub>N<sub>4</sub> NS [32].

The chemical state of the g-C<sub>3</sub>N<sub>4</sub> NS and Co@g-C<sub>3</sub>N<sub>4</sub> NS were studied by FTIR spectroscopy. In the spectra displayed in Fig. 2f, g-C<sub>3</sub>N<sub>4</sub> NS feature a peak at around  $812\text{ cm}^{-1}$ , which can be ascribed to the characteristic breathing mode of tri-s-triazine units, and bands between  $1200\text{ cm}^{-1}$  and  $1680\text{ cm}^{-1}$ , originating from the typical skeletal

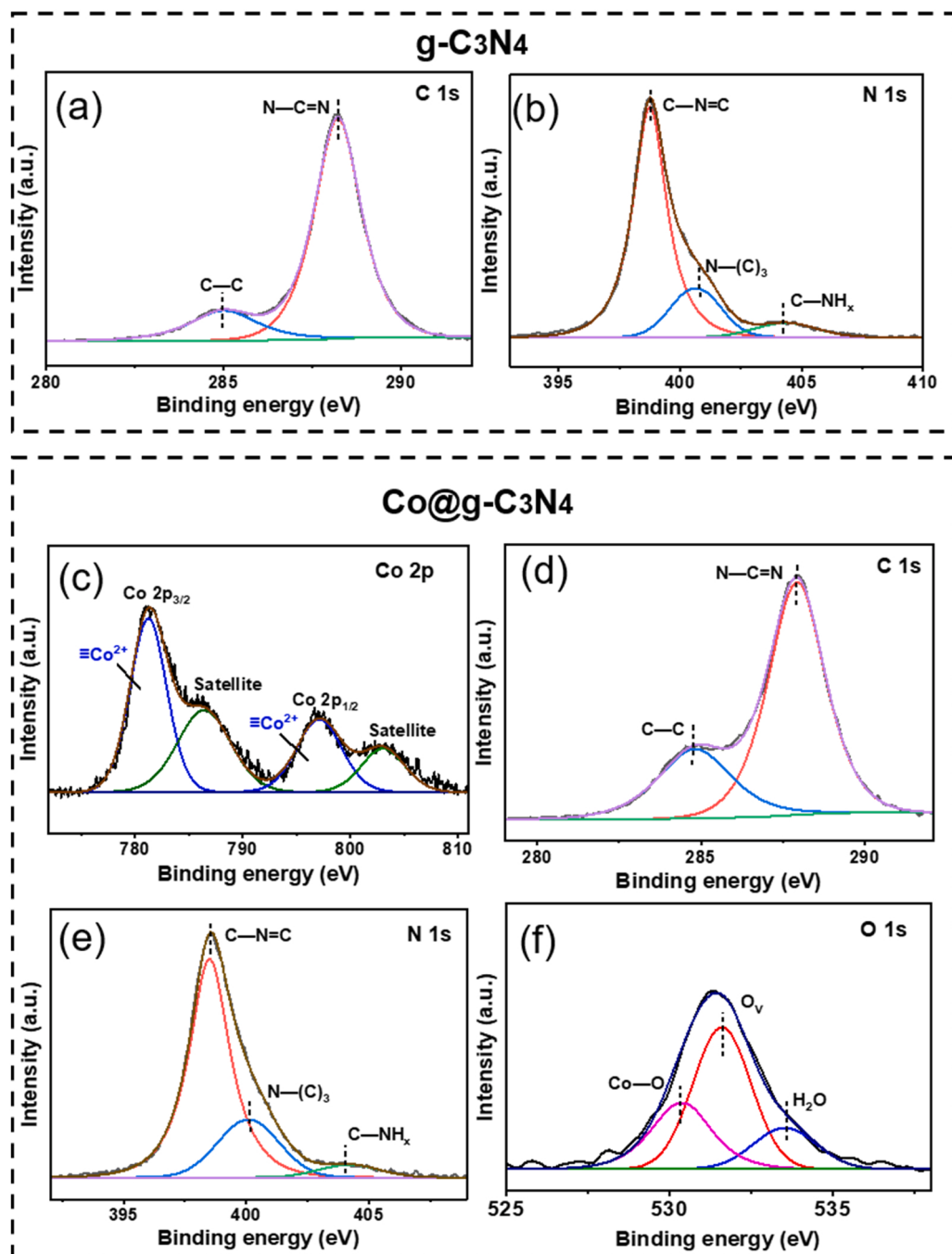


Fig. 3. (a) and (b) XPS spectra of g-C<sub>3</sub>N<sub>4</sub> NS; (c), (d), (e), and (f) XPS spectra of Co@g-C<sub>3</sub>N<sub>4</sub> NS.

vibration modes of CN heterocycles [33]. The broad absorption peak at around  $3200\text{ cm}^{-1}$  was ascribed to the stretching mode of N-H groups [12,22]. For Co@g-C<sub>3</sub>N<sub>4</sub> NS, the peak near  $444\text{ cm}^{-1}$  could be assigned to the stretching vibration of Co-O bonds [22]. All the main characteristic peaks of g-C<sub>3</sub>N<sub>4</sub> were present, indicating that the main chemical structure of g-C<sub>3</sub>N<sub>4</sub> was retained in the Co@g-C<sub>3</sub>N<sub>4</sub> composite, which was consistent with the XRD results.

XPS was performed to determine the specific bonding and chemical states of elements in Co@g-C<sub>3</sub>N<sub>4</sub> NS. The XPS spectra of g-C<sub>3</sub>N<sub>4</sub> NS and Co@g-C<sub>3</sub>N<sub>4</sub> NS are shown in Fig. S2. The C 1 s and N 1 s survey spectrum of g-C<sub>3</sub>N<sub>4</sub> are shown in Fig. 3a and b. The C 1 s spectrum of g-C<sub>3</sub>N<sub>4</sub> contained two dominant component peaks at 284.8 eV and 288.3 eV, which were attributed to C-C and N-C=N bonds. The spectrum of N 1 s had three dominant peaks at 398.8 eV, 400.6 eV, and 404.3 eV, which were ascribed to the C=N-C bond in the triazine rings, N-(C)<sub>3</sub>, and C-NH<sub>x</sub> bonds, respectively [12]. The spectra of g-C<sub>3</sub>N<sub>4</sub> and Co@g-C<sub>3</sub>N<sub>4</sub> shown in Fig. 3c-f confirmed the existence of C, N, O, and Co. The two relatively stronger peaks at 781.3 eV and 797.2 eV were attributed to Co 2p<sub>3/2</sub> and Co 2p<sub>1/2</sub> spin-orbit peaks, respectively, indicating the presence of  $\equiv\text{Co}^{2+}$  (Fig. 3c). The spectrum of Co 2p (Fig. 3c) also revealed two satellite peaks located at 785.8 eV and 803.0 eV, indicating the existence of CoO in Co@g-C<sub>3</sub>N<sub>4</sub> NS [22,34]. In the spectrum in Fig. 3f, three peaks were observed at 530.4 eV, 531.6 eV, and 533.5 eV. The binding energy component in the O 1 s spectrum at 530.4 eV corresponded to Co-O bonds in the CoO phase [22]. The peak at 533.5 eV was associated with absorbed water molecules [35]. The binding energy at 531.6 eV corresponded to oxygen vacancies (O<sub>V</sub>) [36,37]. The oxygen proportion of Co-O, O<sub>V</sub> and absorbed water molecules was 28.3 %, 54.3 % and 17.4 %, respectively. Furthermore, small binding energy shifts were observed in the C 1 s and N 1 s spectrum of Co@g-C<sub>3</sub>N<sub>4</sub> NS (Fig. 3d and e) compared with g-C<sub>3</sub>N<sub>4</sub> NS, which may be caused by the interaction between g-C<sub>3</sub>N<sub>4</sub> NS and CoO nanoparticles.

### 3.2. Characterization of Co@g-C<sub>3</sub>N<sub>4</sub> membranes

The Co@g-C<sub>3</sub>N<sub>4</sub> membrane surface and cross-section morphology were observed by SEM (Fig. 4a and b). According to Fig. 4a, the surface of the Co@g-C<sub>3</sub>N<sub>4</sub> membrane was rough, and the supported catalyst was relatively uniform without cracks. The cross-sectional image (Fig. 4b) of the Co@g-C<sub>3</sub>N<sub>4</sub> membrane revealed a stacked porous structure with an average thickness of about 6  $\mu\text{m}$  at a catalyst loading of 9 mg (0.75 mg/cm<sup>2</sup>), which could provide a high number of nanochannels for the flow of feed solution in the catalytic degradation process. EDS mapping (Fig. 4b) indicated a uniform distribution of the main elements in the Co@g-C<sub>3</sub>N<sub>4</sub> membrane cross-section, including C (41.26 % at%), N (52.18 % at%), Co (1.79 % at%), and O (4.78 % at%).

Co@g-C<sub>3</sub>N<sub>4</sub> membranes were compared in the dry and hydrated state by XRD analysis. For the hydrated membrane, the peak corresponding to the (002) plane moved to a lower angle from  $27.4^\circ$  to  $22.6^\circ$  (Fig. 4c). According to the calculation using Bragg's law, the interlayer spacing (*d*-spacing) of the dry Co@g-C<sub>3</sub>N<sub>4</sub> membrane was 0.33 nm, while that of the hydrated Co@g-C<sub>3</sub>N<sub>4</sub> membrane was 0.39 nm. This indicates that water could pass through the interlayer nanochannels of the Co@g-C<sub>3</sub>N<sub>4</sub> membrane. The specific surface area and pore structure of the Co@g-C<sub>3</sub>N<sub>4</sub> membrane were obtained from the nitrogen absorption-desorption isotherm (Fig. 4d). In this study, the adsorption-desorption isotherm of Co@g-C<sub>3</sub>N<sub>4</sub> samples exhibited a type IV isotherm, indicating the existence of mesoporous structure characteristics in the composite [12]. The specific surface area of Co@g-C<sub>3</sub>N<sub>4</sub> composites was calculated to be  $33.95\text{ m}^2/\text{g}$ . A larger specific surface area promotes the absorption of more reactants and active species on its surface, which is conducive to effectively activate PMS for ROC degradation. The pore size distribution by the Barrett-Joyner-Halenda (BJH) model (inset in Fig. 4d) showed that the pore diameters of the Co@g-C<sub>3</sub>N<sub>4</sub> membrane ranged from 1.75 to 164.61 nm with a peak pore value of 2.24 nm, confirming the existence of intralayer channels. The above results show that the transport of water in the Co@g-C<sub>3</sub>N<sub>4</sub>

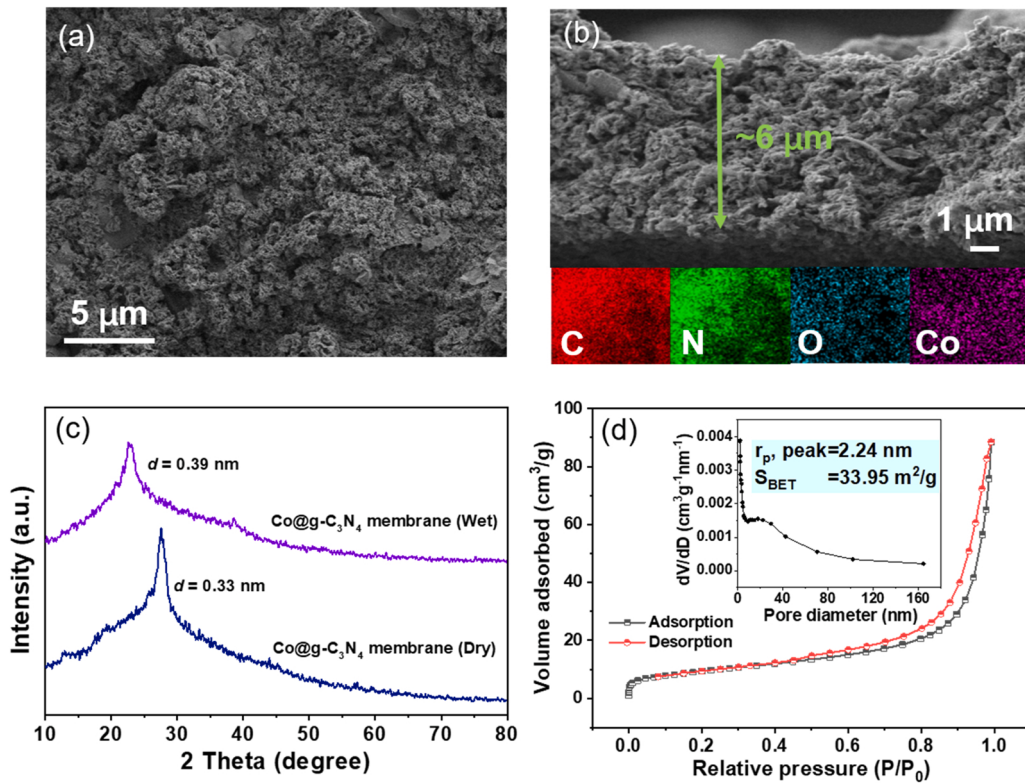


Fig. 4. (a) SEM image of the Co@g-C<sub>3</sub>N<sub>4</sub> membrane surface; (b) SEM image of the Co@g-C<sub>3</sub>N<sub>4</sub> membrane cross-section and EDS mapping image; (c) XRD patterns of wet and dry Co@g-C<sub>3</sub>N<sub>4</sub> membranes; (d) Nitrogen adsorption and desorption isotherm (inset: BJH model pore size distribution curve of the Co@g-C<sub>3</sub>N<sub>4</sub> membrane).

membrane would pass through intralayer channels and interlayer spaces.

### 3.3. Catalytic performance of the $\text{Co}@\text{g-C}_3\text{N}_4$ membrane/PMS system

Ranitidine was selected as a typical organic contaminant to evaluate the catalytic performance of the  $\text{Co}@\text{g-C}_3\text{N}_4$  membrane/PMS system. The catalytic performance of this system was related to the catalyst loading according to Fig. 5a. With increasing  $\text{Co}@\text{g-C}_3\text{N}_4$  membrane catalyst loading from 0.03 to 1.5  $\text{mg}/\text{cm}^2$ , the flux decreased from 226.5 to 97.1  $\text{L}\cdot\text{m}^{-2}\cdot\text{h}^{-1}$ . The increase in catalyst loading enhanced membrane hydrodynamic resistance, resulting in decreased membrane flux. At the same time, catalyst loading affected membrane degradation performance, and 100 % ranitidine removal efficiency was achieved at a catalyst loading of 0.75  $\text{mg}/\text{cm}^2$  (9 mg). Therefore, the catalyst loading of 0.75  $\text{mg}/\text{cm}^2$  was considered to be the most appropriate.

As shown in Fig. 5b, ranitidine could be completely degraded within 30 s in the  $\text{Co}@\text{g-C}_3\text{N}_4$  membrane/PMS system, and the removal efficiency remained stable at 100 % throughout the experimental period. Since a 2D material membrane can remove pollutants through size exclusion and adsorption, further experiments were conducted to investigate such effects on the pollutant removal by the  $\text{Co}@\text{g-C}_3\text{N}_4$  membrane. Nearly 69 % of ranitidine was adsorbed or rejected by the

membrane in three minutes in the absence of PMS. However, the removal efficiency decreased from 69 % to 0 % within 30 min due to adsorption saturation of the membrane. PMS itself demonstrated weak reactivity to ranitidine degradation in the conventional heterogeneous AOP system, and its removal efficiency was only 18.5 % within 30 min. In combination, the above results suggested that ranitidine removal mainly depends on degradation in the  $\text{Co}@\text{g-C}_3\text{N}_4$  membrane/PMS system. The removal efficiency of ranitidine reached 93.3 % in 30 min when the same amount of  $\text{Co}@\text{g-C}_3\text{N}_4$  NS was used as the activator. Thus, the  $\text{Co}@\text{g-C}_3\text{N}_4$  membrane/PMS system showed better degradation performance of ranitidine than its heterogeneous counterpart ( $\text{Co}@\text{g-C}_3\text{N}_4$  NS/PMS) or PMS only. The mineralization efficiency of the  $\text{Co}@\text{g-C}_3\text{N}_4$  membrane/PMS system was 73.4 %, which was significantly higher than that of  $\text{Co}@\text{g-C}_3\text{N}_4$  NS/PMS (39.9 %) or PMS only (8.1 %) systems. The excellent degradation performance of the  $\text{Co}@\text{g-C}_3\text{N}_4$  membrane/PMS system can be attributed to its exposed rich active sites. Meanwhile, the abundant nanochannels in the  $\text{Co}@\text{g-C}_3\text{N}_4$  membrane promote mass transfer, which enables the generated ROS to quickly reach and degrade ranitidine [3,6,8,29]. This can be also proved by the different activation efficiency of PMS in  $\text{Co}@\text{g-C}_3\text{N}_4$  membrane/PMS,  $\text{Co}@\text{g-C}_3\text{N}_4$  NS/PMS and PMS only systems (Text S3). As shown in Fig. S3, the decomposition efficiency of PMS in the  $\text{Co}@\text{g-C}_3\text{N}_4$  membrane/PMS system was 71.4 % after 30 min, which was

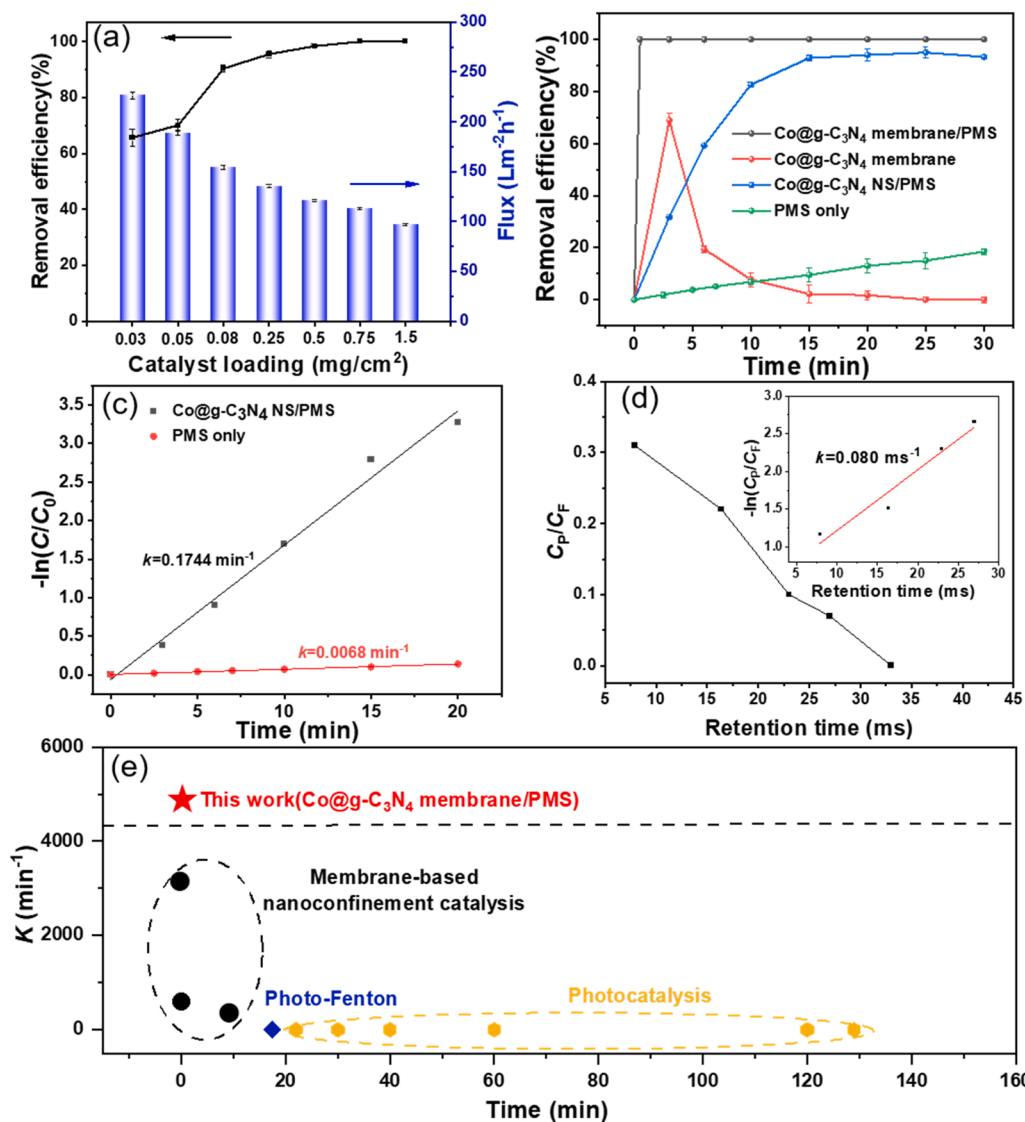


**Fig. 5.** (a) Removal efficiency and flux at different catalyst loadings; (b) Ranitidine removal efficiency with different catalytic systems; (c) First-order rate constants of  $\text{Co}@\text{g-C}_3\text{N}_4$  NS/PMS and PMS only systems; (d) Relationship between ranitidine concentration ( $C_p$  and  $C_F$  correspond to ranitidine concentrations in the permeated solution and feed solution, respectively) and retention time (inset: first-order rate constant of ranitidine removal). (e) Comparison of the first-order rate constants ( $k$ ) of different systems. Conditions: [ranitidine] = 5  $\text{mg}/\text{L}$ , [PMS] = 0.16  $\text{mM}$ , initial pH = 4.0, temperature = 25  $^{\circ}\text{C}$ .

significantly higher than the other two systems (38.2 % for Co@g-C<sub>3</sub>N<sub>4</sub> NS/PMS system and 15.2 % for PMS only system).

The catalytic performance of the Co@g-C<sub>3</sub>N<sub>4</sub> membrane was further analyzed according to retention time, which was calculated using the internal volume, water flux of the membrane, effective filtration area, and total mass of the membrane (Text S4). The results showed that ranitidine could be completely removed by the Co@g-C<sub>3</sub>N<sub>4</sub> membrane/PMS system with a solution retention time of about 33 ms (Fig. 5d). It is worth noting that the first-order rate constant of the Co@g-C<sub>3</sub>N<sub>4</sub> membrane/PMS system (inset in Fig. 5d) reached 0.080 ms<sup>-1</sup>. As indicated in Fig. 5c, the first-order rate constants of the conventional heterogeneous Co@g-C<sub>3</sub>N<sub>4</sub> NS/PMS system and the PMS-only system were 0.1744 min<sup>-1</sup> and 0.0068 min<sup>-1</sup>, respectively. The first-order rate constant of the Co@g-C<sub>3</sub>N<sub>4</sub> membrane/PMS system was 4–6 orders of magnitude higher than that of the Co@g-C<sub>3</sub>N<sub>4</sub> NS/PMS and PMS-only systems, demonstrating its efficient ability for ranitidine degradation. Furthermore, the Co@g-C<sub>3</sub>N<sub>4</sub> membrane/PMS system showed a 10<sup>4</sup>–10<sup>6</sup> times higher ranitidine degradation rate than the rates of previously reported photocatalytic systems (0.0032–0.23 min<sup>-1</sup>, Fig. 5e and Table S2). In addition, the Co@g-C<sub>3</sub>N<sub>4</sub> membrane/PMS system also has certain advantages (1.5–43 times faster) compared with the reported membrane-based nanoconfined catalysis systems (Fig. 5e and Table S2).

#### 3.4. Effect of operating conditions on degradation performance of the Co@g-C<sub>3</sub>N<sub>4</sub> membrane/PMS system

The Co@g-C<sub>3</sub>N<sub>4</sub> membrane/PMS system was operated in continuous flow mode to test the stability of its degradation efficiency. The efficiency of ranitidine decomposition remained 100% after 100 h of

continuous flow operation (Fig. 6a). It was observed that the water flux through the Co@g-C<sub>3</sub>N<sub>4</sub> membrane fluctuated slightly during operation, but the overall performance remained stable. This excellent stability originates from its exposed abundant active sites. CoO nanoparticles were evenly distributed on the g-C<sub>3</sub>N<sub>4</sub> surface, which avoids the aggregation of CoO nanoparticles and protects them from inactivation [22]. Cobalt leaching during membrane operation may affect the stability of the membrane and may easily cause secondary pollution. The cobalt leaching concentration measured in the permeate of the Co@g-C<sub>3</sub>N<sub>4</sub> membrane was 5.64 µg/L after operating the system for 100 h (Table S3), which was lower than the World Health Organization (WHO) benchmark for drinking water quality, i.e., 10 µg/L. Therefore, the Co@g-C<sub>3</sub>N<sub>4</sub> membrane/PMS system is stable and efficient for the degradation of organic contaminants in wastewater.

In actual wastewater treatment processes, the composition of polluted water bodies is complex. The impact of different pH and anions on the Co@g-C<sub>3</sub>N<sub>4</sub> membrane/PMS system was investigated. The effect of pH on ranitidine degradation was studied by changing the initial solution pH from 4.0 to 10.0. As shown in Fig. 6b, when the initial pH was 10.0, the removal efficiency of ranitidine after 30 min was only 49.03 %. As the initial pH decreased to 8.0, 6.0, and 4.0, the removal efficiency increased sharply to 97.57 %, 96.62 %, and 100 %, respectively. Solution pH may affect the speciation of the ROS, thus affecting pollutant degradation [38]. Under neutral pH conditions, organic pollutants are degraded equally by SO<sub>4</sub><sup>2-</sup> and •OH [39]. However, SO<sub>4</sub><sup>2-</sup> is dominant when pH is lower than 7.0, and SO<sub>4</sub><sup>2-</sup> exhibits higher redox potential than •OH [38]. Compared with the degradation efficiency observed at pH 10, the removal efficiency of the Co@g-C<sub>3</sub>N<sub>4</sub> membrane/PMS system at pH 4 increased by approximately 50 % (Fig. 6b).

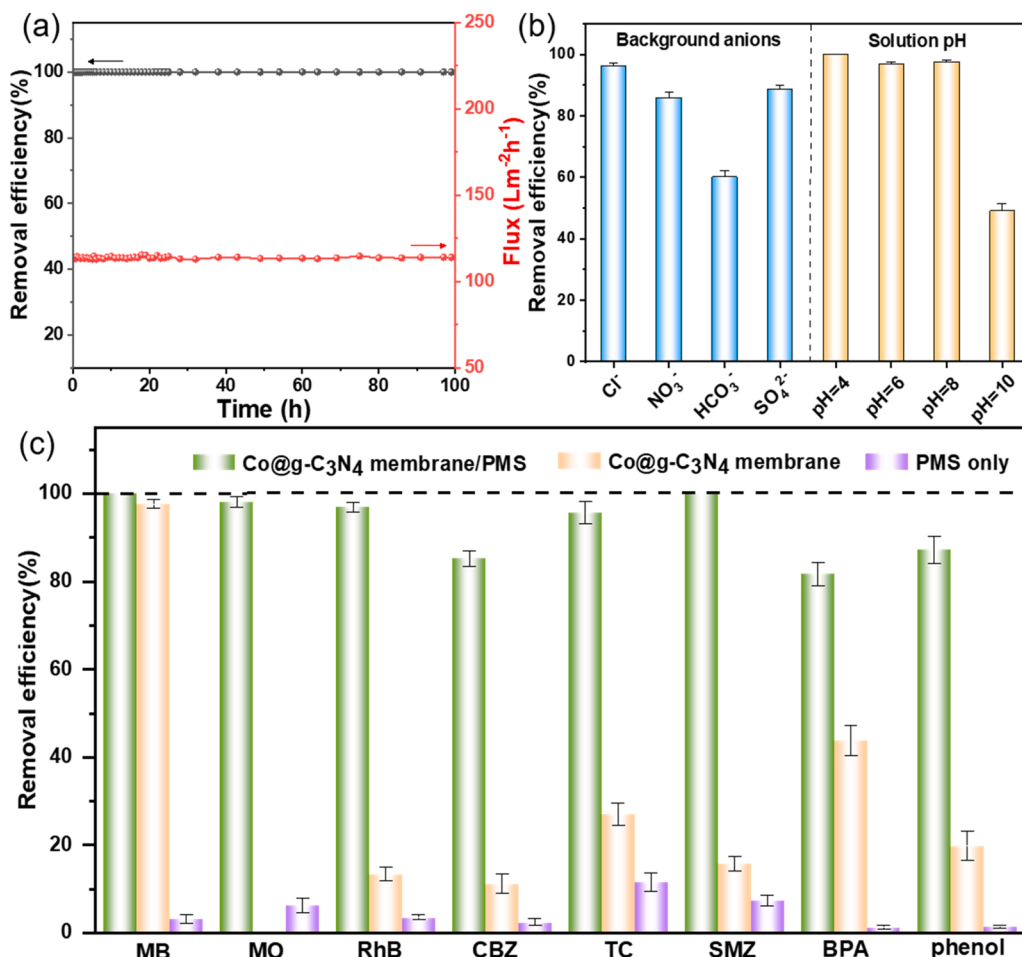


**Fig. 6.** (a) Ranitidine removal efficiency and flux variations of the Co@g-C<sub>3</sub>N<sub>4</sub> membrane/PMS system with running time; (b) Effects of solution pH and background anions on ranitidine removal by Co@g-C<sub>3</sub>N<sub>4</sub> membrane/PMS; (c) Removal efficiency of various organic pollutants by the PMS-only, the Co@g-C<sub>3</sub>N<sub>4</sub> membrane, and the Co@g-C<sub>3</sub>N<sub>4</sub> membrane/PMS systems. Conditions: [ranitidine] or [other pollutants] = 5 mg/L, [PMS] = 0.16 mM, initial pH = 4.0, [anions] = 5 mM, temperature = 25 °C.

Chloride ( $\text{Cl}^-$ ), nitrate ( $\text{NO}_3^-$ ), bicarbonate ( $\text{HCO}_3^-$ ), and sulfate ions ( $\text{SO}_4^{2-}$ ) were added separately to the  $\text{Co}@\text{g-C}_3\text{N}_4$  membrane/PMS system at a concentration of 5 mM to evaluate their impact on ranitidine removal. The addition of these four anions had an obvious effect on the system, reducing the removal efficiency of ranitidine by 4–40 %. The addition of  $\text{Cl}^-$  had a weak effect on ranitidine degradation, and the removal efficiency only decreased to 96.04 %.  $\text{Cl}^-$  was oxidized to low-active chlorine or hypochlorite by  $\bullet\text{OH}$  and  $\text{SO}_4^{2-}$ , showing inhibitory effects [7,29].  $\text{NO}_3^-$  and  $\text{SO}_4^{2-}$  exhibited highly negative impacts on the removal efficiency of ranitidine, reducing it to 85.78 % and 88.61 %, respectively. The effect of  $\text{NO}_3^-$  on ranitidine degradation was attributed to  $\text{NO}_3^-$  consuming  $\text{SO}_4^{2-}$  with high redox potential and producing  $\text{NO}_3^-$  and  $\text{NO}_2^-$ , which are species of low activity [19,40]. It has been reported that  $\text{SO}_4^{2-}$  can also react with  $\bullet\text{OH}$ , which may be the reason for hindering ranitidine degradation [41]. Among the anions,  $\text{HCO}_3^-$  had the greatest negative effects on ranitidine degradation, reducing its removal efficiency by 40 %. This could be attributed to the buffering effect of  $\text{HCO}_3^-$  on the solution, which would increase the solution pH [42]. Furthermore,  $\text{HCO}_3^-$  could be used as the quencher and consume  $\bullet\text{OH}$  and  $\text{SO}_4^{2-}$  [43,44]. In summary, anions mainly affect the degradation performance of the system through the transformation of reactive oxygen species [45].

The degradation performance of the  $\text{Co}@\text{g-C}_3\text{N}_4$  membrane/PMS system was further investigated by using the real water matrix including tap water and lake water. As shown in Fig. S4, the removal efficiency of ranitidine in tap water by the  $\text{Co}@\text{g-C}_3\text{N}_4$  membrane/PMS system reached 86.8 % after 30 min, which could be attributed to the residual chlorine in tap water. In lake water, the removal efficiency of ranitidine by the  $\text{Co}@\text{g-C}_3\text{N}_4$  membrane/PMS system was 77.8 % after 30 min. The lake water contains complex natural organic matters (NOM) and anions (Table S4), both of which would contribute to the deteriorated degradation performance. The inhibition effects of anions have been discussed

in Fig. 6b. NOM can eliminate hydroxyl radical and sulfate radical [7], meanwhile, phenolic hydroxyl and carboxyl contained in NOM may be adsorbed onto the catalyst surface and prevent PMS from contacting the active sites of catalyst [7,46].

Fig. 6c shows the removal efficiency of the PMS-only, the  $\text{Co}@\text{g-C}_3\text{N}_4$  membrane, and the  $\text{Co}@\text{g-C}_3\text{N}_4$  membrane/PMS systems for various organic pollutants, including three dyes (methyl orange (MO), methylene blue (MB), and rhodamine B (RhB)), three PPCPs (carbamazepine (CBZ), tetracycline hydrochloride (TC), and sulfamethoxazole (SMZ)) and two phenols (bisphenol A (BPA) and phenol). The removal efficiency of MB, MO, RhB, CBZ, TC, SMZ, BPA, and phenol by the  $\text{Co}@\text{g-C}_3\text{N}_4$  membrane/PMS system reached 100 %, 98.1 %, 97.0 %, 85.2 %, 95.7 %, 100 %, 81.7 %, and 87.2 %, respectively. However, the removal efficiency of multiple pollutants by PMS alone was between 1.3 % and 11.6 %. Except for a removal efficiency of MB of 97.6 %, the  $\text{Co}@\text{g-C}_3\text{N}_4$  membrane system removed the other seven pollutants only between 0 % and 43.9 % after 30 min. Therefore, the  $\text{Co}@\text{g-C}_3\text{N}_4$  membrane/PMS system can effectively degrade many types of organic pollutants.

### 3.5. Degradation mechanism in the $\text{Co}@\text{g-C}_3\text{N}_4$ membrane/PMS system

#### 3.5.1. Identification and contribution of ROS

The  $\text{Co}@\text{g-C}_3\text{N}_4$  membrane/PMS system showed excellent pollutant degradability in this study, and it is important to clarify the AOP mechanisms by identifying the ROS and their contribution. EPR experiments using the spin-trapping agents TEMP and 5,5-dimethyl-1-pyrroline (DMPO) were performed to detect the existence of  $^1\text{O}_2$  and  $\text{SO}_4^{2-}/\bullet\text{OH}$  in the  $\text{Co}@\text{g-C}_3\text{N}_4$  membrane/PMS system, respectively. When the trapping agent of TEMP was applied, the TEMP- $^1\text{O}_2$  adduct was detected (height ratio = 1:1:1, hyperfine coupling constant  $a_N = 16.9$  G), which indicates the formation of  $^1\text{O}_2$  (Fig. 7a). The EPR spectrum in Fig. 7b showed the signal of the DMPO- $\bullet\text{OH}$  adduct (height ratio = 1:2:2:1,

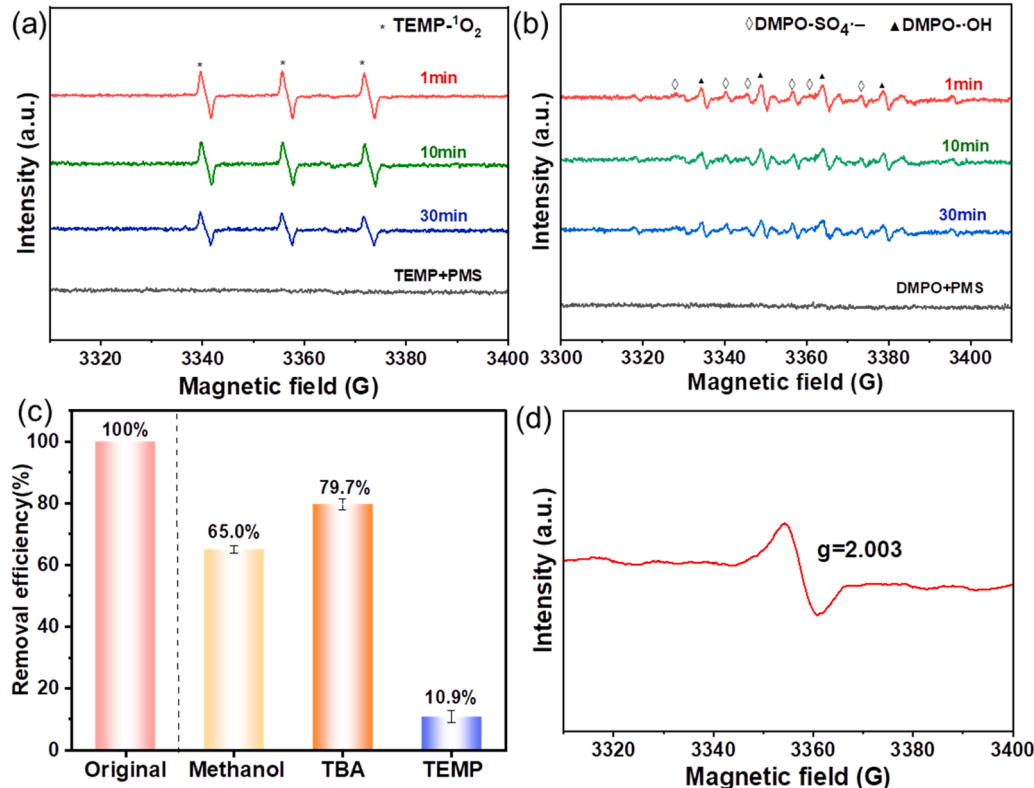


Fig. 7. (a) EPR spectra of TEMP- $^1\text{O}_2$  in the  $\text{Co}@\text{g-C}_3\text{N}_4$  membrane/PMS system; (b) EPR spectra of DMPO- $\bullet\text{OH}$  adduct in the  $\text{Co}@\text{g-C}_3\text{N}_4$  membrane/PMS system; (c) Ranitidine removal efficiency under different quenching conditions; (d) EPR test for oxygen vacancies in solid  $\text{Co}@\text{g-C}_3\text{N}_4$  NS. Conditions: [ranitidine] = 5 mg/L, [PMS] = 0.16 mM, initial pH = 4.0, temperature = 25 °C, and (a) [TEMP] = 50 mM or (b) [DMPO] = 0.3 mM.

hyperfine coupling constants  $a_N = a_H = 14.9$  G) when using DMPO as the trapping agent in the  $\text{Co@g-C}_3\text{N}_4$  membrane/PMS system. The signal of DMPO- $\text{SO}_4^{\cdot-}$  adduct (hyperfine coupling constants  $a_N = 13.2$  G,  $a_H = 9.6$  G,  $a_H = 1.48$  G and  $a_H = 0.78$  G) was also observed in the EPR experiment. It is reported that DMPO has a stronger ability to trap  $\bullet\text{OH}$ , and the signal of DMPO- $\bullet\text{OH}$  adduct is usually higher than that of DMPO- $\text{SO}_4^{\cdot-}$  adduct [47,48]. Therefore, the signal of DMPO- $\text{SO}_4^{\cdot-}$  adduct was not prominent in this work. The above results proved that  $\text{Co@g-C}_3\text{N}_4$  membrane/PMS produced the reactive species  $\bullet\text{OH}$ ,  $\text{SO}_4^{\cdot-}$  and  ${}^1\text{O}_2$  during the degradation of ranitidine.

To reveal the contribution of different ROS for ranitidine degradation in the  $\text{Co@g-C}_3\text{N}_4$  membrane/PMS system, the quenching tests were then conducted with different quenchers. TBA served as a radical scavenger for  $\bullet\text{OH}$ , while MeOH was employed as a quencher for both  $\bullet\text{OH}$  and  $\text{SO}_4^{\cdot-}$ . TEMP was selected as the quenching agent for  ${}^1\text{O}_2$ . As shown in Fig. 7c, when TBA was added to the  $\text{Co@g-C}_3\text{N}_4$  membrane/PMS system, ranitidine removal efficiency decreased to 79.7%. When

MeOH was added to this system, the ranitidine removal efficiency declined to 65.0% (Fig. 7c). These results indicated that neither  $\bullet\text{OH}$  and nor  $\text{SO}_4^{\cdot-}$  were the main oxidants. The addition of TEMP, however, had an obvious inhibitory effect on ranitidine degradation, and the removal efficiency decreased to 10.9%, implying that non-radical  ${}^1\text{O}_2$  significantly contributed to ranitidine degradation.

To further verify the existence of oxygen vacancies in  $\text{Co@g-C}_3\text{N}_4$  NS, EPR tests were conducted on this material. An obvious symmetrical signal ( $g = 2.003$ ) was present in the EPR spectrum of the  $\text{Co@g-C}_3\text{N}_4$  NS sample (Fig. 7d), indicating the existence of oxygen vacancies. This result was consistent with the above XPS characterization results (Fig. 3f). The introduction of oxygen vacancies can effectively improve charge transfer ability, thus promoting catalytic reactions [49]. Studies have shown that oxygen vacancies can promote the redox cycle of cobalt ions ( $\equiv\text{Co(II)}/\equiv\text{Co(III)}$ ) to maintain the catalytically active center [50].

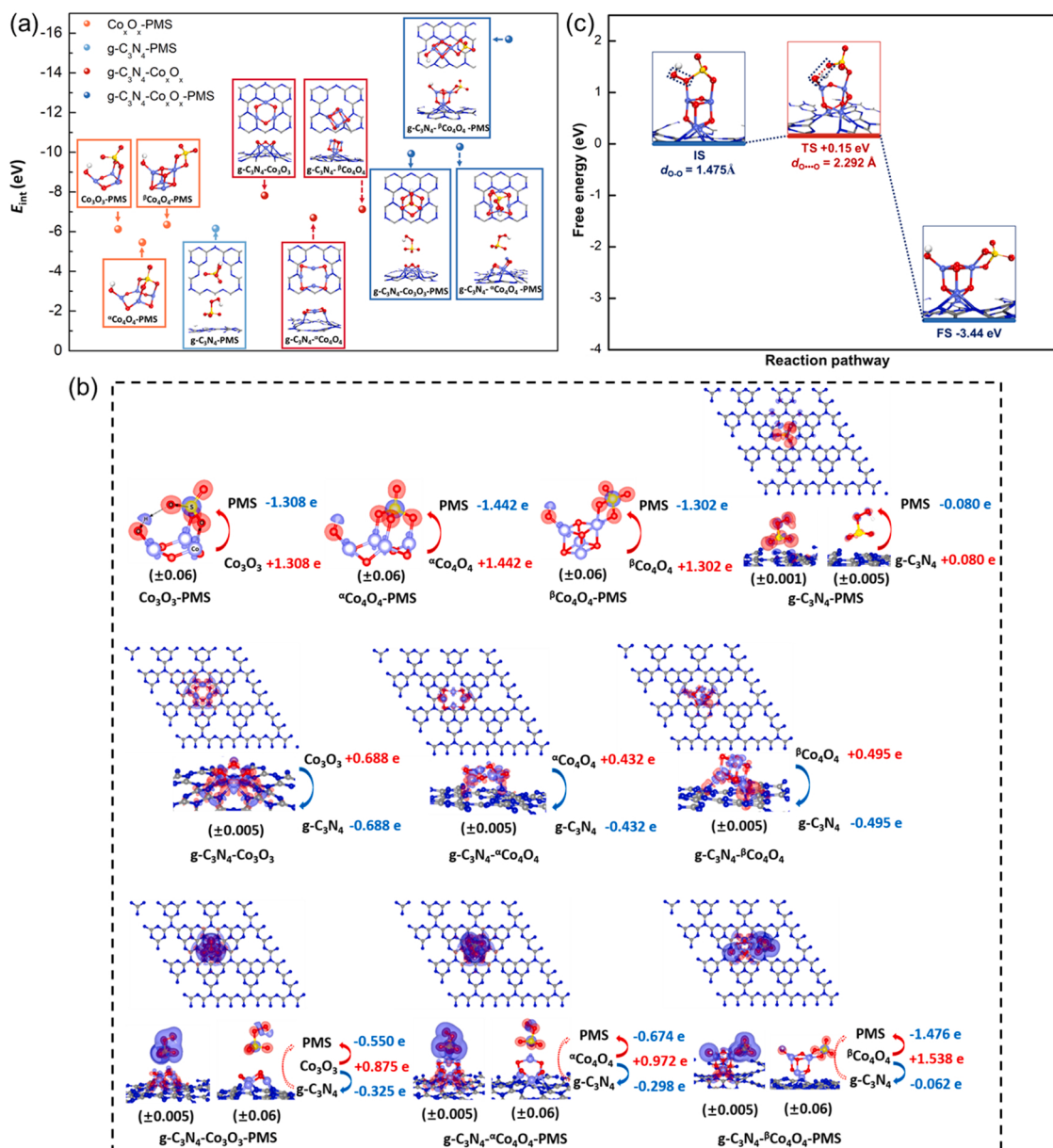


**Fig. 8.** (a) Interaction energies ( $E_{\text{int}}$ ) and geometries of the studied systems; (b) Electron density difference (EDD) diagrams for studied systems; The Bader populations are labeled for different fragments (PMS,  $\text{Co}_x\text{O}_x$ , and  $\text{g-C}_3\text{N}_4$ ) of each system. The red and blue isosurfaces represent electronic accumulation and depletion, respectively. The values of isosurfaces are given below the lateral view of the EDD pictures; (c) Energy profile during the process of PMS dissociation.

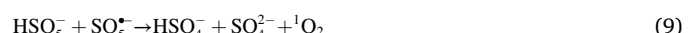
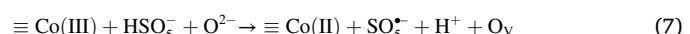
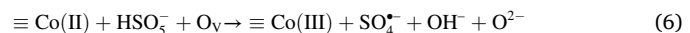
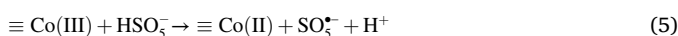
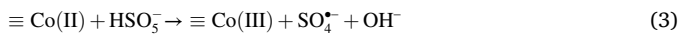
### 3.5.2. Mechanisms of PMS activation and electron transport

DFT calculations were performed to assess the adsorption behavior of PMS molecules on the g-C<sub>3</sub>N<sub>4</sub>-Co<sub>x</sub>O<sub>x</sub> substrate. A g-C<sub>3</sub>N<sub>4</sub> network of hexagonal pattern was constructed in this work. Three types of Co<sub>x</sub>O<sub>x</sub> clusters, Co<sub>3</sub>O<sub>3</sub>,  $\alpha$ -Co<sub>4</sub>O<sub>4</sub>, and  $\beta$ -Co<sub>4</sub>O<sub>4</sub>, were optimized, and the structures are depicted in Fig. S5. The interaction energies ( $E_{\text{int}}$ ) between PMS, Co<sub>x</sub>O<sub>x</sub>, and g-C<sub>3</sub>N<sub>4</sub> were calculated (Text S2).

The energetic and geometric data are summarized in Fig. 8a, and only the interaction regions are shown for clarity. During the adsorption process of the PMS molecule on Co<sub>x</sub>O<sub>x</sub>, the O-O bond of the PMS molecule is broken. The interaction of the cubic structure of the  $\beta$ -Co<sub>4</sub>O<sub>4</sub> cluster was calculated to be stronger than that of the planar structure of the Co<sub>3</sub>O<sub>3</sub> and  $\alpha$ -Co<sub>4</sub>O<sub>4</sub> clusters. For g-C<sub>3</sub>N<sub>4</sub>, the PMS molecule tends to be adsorbed on the hollow site of g-C<sub>3</sub>N<sub>4</sub> because more active sites should be provided from N atoms of g-C<sub>3</sub>N<sub>4</sub>, while the PMS molecule is stable on the g-C<sub>3</sub>N<sub>4</sub> surface. Then, PMS molecule was added to the Co<sub>x</sub>O<sub>x</sub> @g-C<sub>3</sub>N<sub>4</sub> systems to mimic a more realistic experimental environment. The  $E_{\text{int}}$  of the Co<sub>x</sub>O<sub>x</sub> @g-C<sub>3</sub>N<sub>4</sub>-PMS systems (especially the  $\beta$ -Co<sub>4</sub>O<sub>4</sub> @g-C<sub>3</sub>N<sub>4</sub> system) was much higher than that of the Co<sub>x</sub>O<sub>x</sub>-PMS and g-C<sub>3</sub>N<sub>4</sub>-PMS systems. The PMS molecular structure in the Co<sub>3</sub>O<sub>3</sub> @g-C<sub>3</sub>N<sub>4</sub> and  $\alpha$ -Co<sub>4</sub>O<sub>4</sub> @g-C<sub>3</sub>N<sub>4</sub> systems is stable, however, PMS dissociates through the cleavage of its O-O bond in the  $\beta$ -Co<sub>4</sub>O<sub>4</sub> @g-C<sub>3</sub>N<sub>4</sub> system. The geometries of the Co<sub>3</sub>O<sub>3</sub> and  $\alpha$ -Co<sub>4</sub>O<sub>4</sub> clusters are not parallel to the planar structure when they adsorb on the g-C<sub>3</sub>N<sub>4</sub> surface because the Co-N bonds are formed and the Co atoms are slightly moved from the original Co<sub>x</sub>O<sub>x</sub> plane. As a consequence, the Co atom can hardly attract the oxygen atom of the PMS molecule, and the O-O bond of PMS tends to be stable in the adsorption process. In the involved cubic  $\beta$ -Co<sub>4</sub>O<sub>4</sub> cluster system, two Co atoms near the g-C<sub>3</sub>N<sub>4</sub> surface are moved away from the whole cubic structure, while the upper two Co atoms can activate PMS through the cleavage of its O-O bond.

To gain a better understanding from a charge transfer perspective, qualitative electron density difference (EDD) and quantitative Bader population analyses were performed (Text S2). The 3D colored EDD plot is provided in Fig. 8b, in which the red and blue isosurfaces represent electronic accumulation and depletion, respectively. For the Co<sub>x</sub>O<sub>x</sub>-PMS system, a large charge transfer (from 1.302 e to 1.442 e) was observed from Co<sub>x</sub>O<sub>x</sub> clusters to PMS molecules. The small charge redistribution detected between g-C<sub>3</sub>N<sub>4</sub> and PMS (0.080 e) indicated that the nature of interactions in this system is mainly dominated by Van der Waals forces but not by electrostatic forces. In the g-C<sub>3</sub>N<sub>4</sub>-Co<sub>x</sub>O<sub>x</sub> system, the charge transfer amounts from Co<sub>3</sub>O<sub>3</sub>,  $\alpha$ -Co<sub>4</sub>O<sub>4</sub>, and  $\beta$ -Co<sub>4</sub>O<sub>4</sub> to the g-C<sub>3</sub>N<sub>4</sub> substrate are 0.688 e, 0.432 e, and 0.495 e, respectively. When PMS interacts with g-C<sub>3</sub>N<sub>4</sub>-Co<sub>x</sub>O<sub>x</sub>, the charge tends to be transferred from the Co<sub>x</sub>O<sub>x</sub> cluster to PMS and the g-C<sub>3</sub>N<sub>4</sub> substrate, and the value of the former (from Co<sub>x</sub>O<sub>x</sub> to PMS) is computed to be larger than the latter (from Co<sub>x</sub>O<sub>x</sub> to g-C<sub>3</sub>N<sub>4</sub>). As shown in Fig. 8b, a charge of 1.538 e is transferred from  $\beta$ -Co<sub>4</sub>O<sub>4</sub> to PMS (1.476 e) and g-C<sub>3</sub>N<sub>4</sub> (0.062 e). It is clear that the vast majority of electronic redistribution has occurred between  $\beta$ -Co<sub>4</sub>O<sub>4</sub> and PMS with the dissociation of PMS through the cleavage of its O-O bond in the  $\beta$ -Co<sub>4</sub>O<sub>4</sub> @g-C<sub>3</sub>N<sub>4</sub>-PMS system.

To illustrate the mechanism of PMS dissociation on g-C<sub>3</sub>N<sub>4</sub>- $\beta$ -Co<sub>4</sub>O<sub>4</sub>, Climbing Nudged Elastic Band (CINEB) calculations were performed on the same theoretical level of optimization calculations. As shown in Fig. 8c, a transition state (+0.15 eV) with a longer O-O distance compared to the O-O bond of the initial state (2.292 Å versus 1.475 Å) is present, indicating that the dissociation of PMS should be attributed to the bond breaking of the O-O bond. Moreover, the dissociation of PMS on g-C<sub>3</sub>N<sub>4</sub>- $\beta$ -Co<sub>4</sub>O<sub>4</sub> is thermodynamically favorable with a free energy of  $\sim$  3.44 eV.



Based on the above results, the degradation mechanisms are divided into two pathways, a radical process and a non-radical process. The activation of PMS depends on electron transfer, which occurs from Co@g-C<sub>3</sub>N<sub>4</sub> to PMS [51]. In the radical process,  $\equiv$ Co(II) as the active site reacted with HSO<sub>5</sub><sup>-</sup> and transferred one electron to PMS for SO<sub>4</sub><sup>2-</sup> production (Eq. (3)).  $\bullet$ OH could be produced by hydrolysis of SO<sub>4</sub><sup>2-</sup> (Eq. (4)).  $\equiv$ Co(III) could oxidize HSO<sub>5</sub><sup>-</sup> to SO<sub>5</sub><sup>2-</sup> and be reduced to  $\equiv$ Co(II) (Eq. (5)). The cycle of  $\equiv$ Co(II)/ $\equiv$ Co(III) was the main reason for the long-term high-efficiency stability of the Co@g-C<sub>3</sub>N<sub>4</sub> membrane/PMS system. The activation mechanism of PMS was further understood by comparing the XPS spectra before and after the 100 h stability test (Fig. S6). When comparing the proportion of cobalt species before and after the stability test (Table S5), about 34.4%  $\equiv$ Co(II) was converted to  $\equiv$ Co(III). Meanwhile, Co@g-C<sub>3</sub>N<sub>4</sub> containing oxygen vacancies promoted the electron transfer between cobalt ion and PMS, accelerating the cycle of  $\equiv$ Co(II)/ $\equiv$ Co(III) and improving catalytic activity. O<sub>v</sub> and O<sup>2-</sup> represented oxygen vacancy and oxygen ions in normal oxygen position, respectively. The involvement of oxygen vacancies for PMS activation is shown in Eq. 6. Oxygen vacancies promoted the cycle of  $\equiv$ Co(II)/ $\equiv$ Co(III) (Eqs. (6) and (7)), while the regeneration of active sites was the key to maintaining the catalytic stability of the Co@g-C<sub>3</sub>N<sub>4</sub> membrane [50]. In the non-radical process, the reaction between H<sub>2</sub>O and SO<sub>5</sub><sup>2-</sup> may produce <sup>1</sup>O<sub>2</sub>, and electron transfer promoted the self-decomposition of PMS to generate more <sup>1</sup>O<sub>2</sub> (Eqs. (8) and (9)) [52]. The <sup>1</sup>O<sub>2</sub> generation pathway also involved oxygen vacancies and was divided into two steps. O<sub>v</sub> was first converted to O<sup>2-</sup> and then reacted directly with HSO<sub>5</sub><sup>-</sup> to produce <sup>1</sup>O<sub>2</sub> (Eqs. (10) and (11)) [53]. The ROS (SO<sub>4</sub><sup>2-</sup>,  $\bullet$ OH, and <sup>1</sup>O<sub>2</sub>) produced by the Co@g-C<sub>3</sub>N<sub>4</sub> membrane/PMS system directly degraded pollutants (Eq. (12)).

LC-MS was adopted to explore the intermediates and degradation pathways of ranitidine in the Co@g-C<sub>3</sub>N<sub>4</sub> membrane/PMS system. As shown in Fig. S7 and Table S6, ranitidine (*m/z* = 315) was degraded into a series of small molecular intermediates as the reaction proceeded. Meanwhile, two possible degradation pathways of ranitidine were proposed (Fig. S8) based on the analysis of the LC-MS results (Fig. S7). Pathway I: ranitidine was attacked by ROS, leading to N-dealkylation of ranitidine with the production of P8 (*m/z* = 302). P8 further degraded to P6 (*m/z* = 250) through oxygen addition and hydroxylation. Pathway II: ROS attacked ranitidine to produce P3 (*m/z* = 192) and P4 (*m/z* = 214) through bond cleavage. P3 and P4 further degraded to P1 (*m/z* = 111), P2 (*m/z* = 163), P7 (*m/z* = 280) and P5 (*m/z* = 228) respectively through oxygen addition/hydroxylation. Finally, ranitidine degradation intermediates were further degraded to H<sub>2</sub>O, CO<sub>2</sub> and small molecule organics.

## 4. Conclusion

In conclusion, Co@g-C<sub>3</sub>N<sub>4</sub> NS are excellent 2D materials for the fabrication of catalytic membranes. The removal efficiency of ranitidine by the Co@g-C<sub>3</sub>N<sub>4</sub> membrane can reach 100% with a flux and membrane retention time of 113.2 L•m<sup>-2</sup>•h<sup>-1</sup> and 33 ms, respectively. The

Co@g-C<sub>3</sub>N<sub>4</sub> membrane maintained stable ranitidine degradation efficiency over 100 h of continuous flow operation. This membrane has also been demonstrated to be effective for the degradation of a variety of refractory pollutants, including PPCPs, dyes, and phenols. Sulfate radicals, hydroxyl radicals, and singlet oxygen were detected during PMS activation. Singlet oxygen significantly contributes to pollutant degradation. The pores and intralayer/interlayer channels in the membrane provide many catalytically active sites for the AOP reaction. Nanoconfined spaces in the Co@g-C<sub>3</sub>N<sub>4</sub> membrane greatly shorten the mass transfer distance between ROS and pollutants, improving catalytic efficiency. The oxygen vacancies on Co@g-C<sub>3</sub>N<sub>4</sub> promote the redox cycle of  $\equiv$ Co(II)/ $\equiv$ Co(III), thus achieving catalytic stability. DFT calculations indicate that charge transfer has occurred from cobalt(II) oxide to PMS with the dissociation of PMS through the cleavage of its O-O bond and the dissociation of PMS is thermodynamically favorable. The Co@g-C<sub>3</sub>N<sub>4</sub> membrane/PMS system shows efficient and stable wastewater treatment performance, which provides a novel strategy for traditional heterogeneous catalytic systems.

#### CRediT authorship contribution statement

**Wei Zhang:** Writing – original draft preparation, Conceptualization, Methodology, Visualization, Investigation. **Shaoze Zhang:** Methodology, Visualization, Investigation. **Chenchen Meng:** Methodology, Visualization. **Zhenghua Zhang:** Supervision, Conceptualization, Validation, Writing – review & editing, Funding acquisition.

#### Declaration of Competing Interest

The authors declare that they have no known competing financial interests or personal relationships that could have appeared to influence the work reported in this paper.

#### Data Availability

Data will be made available on request.

#### Acknowledgments

This work was financially supported by the National Natural Science Foundation of China (52170041), Tsinghua SIGS Start-up Funding (QD2020002N), and the Committee of Science and Technology Innovation of Shenzhen (JCYJ20190813163401660).

#### Appendix A. Supporting information

Supplementary data associated with this article can be found in the online version at [doi:10.1016/j.apcatb.2022.122098](https://doi.org/10.1016/j.apcatb.2022.122098).

#### References

- S. Rojas, P. Horcada, Metal–organic frameworks for the removal of emerging organic contaminants in water, *Chem. Rev.* 120 (2020), <https://doi.org/10.1021/acs.chemrev.9b00797>.
- F.I. Vacchi, J.A. de S. Vendemiatti, B.F. da Silva, M.V.B. Zanoni, G. de A. Umbuzeiro, Quantifying the contribution of dyes to the mutagenicity of waters under the influence of textile activities, *Sci. Total Environ.* 601–602 (2017) 230–236, <https://doi.org/10.1016/j.scitotenv.2017.05.103>.
- Z. Wang, C. Meng, W. Zhang, S. Zhang, B. Yang, Z. Zhang, Honeycomb-like holey Co<sub>3</sub>O<sub>4</sub> membrane triggered peroxymonosulfate activation for rapid degradation of organic contaminants, *Sci. Total Environ.* 814 (2022), 152698, <https://doi.org/10.1016/j.scitotenv.2021.152698>.
- D. Ghime, P. Ghosh, Advanced Oxidation Processes: A Powerful Treatment Option for the Removal of Recalcitrant Organic Compounds, in: 2020: pp. 1–12. DOI: 10.5772/intechopen.90192.
- J. Pu, J. Wan, Y. Wang, Y. Ma, Different Co-based MOFs templated synthesis of Co<sub>3</sub>O<sub>4</sub> nanoparticles to degrade RhB by activation of oxone, *RSC Adv.* 6 (2016) 91791–91797, <https://doi.org/10.1039/C6RA15590A>.
- C. Meng, B. Ding, S. Zhang, L. Cui, K. Ostrrikov, Z. Huang, B. Yang, J. Kim, Z. Zhang, Angstrom-confined catalytic water purification within Co-TiO<sub>x</sub> laminar membrane nanochannels, *Nat. Commun.* 13 (2022) 4010, <https://doi.org/10.1038/s41467-022-31807-1>.
- P. Hu, M. Long, Cobalt-catalyzed sulfate radical-based advanced oxidation: a review on heterogeneous catalysts and applications, *Appl. Catal. B: Environ.* 181 (2016) 103–117, <https://doi.org/10.1016/j.apcatb.2015.07.024>.
- C. Meng, Z. Wang, W. Zhang, B. Yang, H. Xie, Z. Zhang, Laminar membranes assembled by ultrathin cobalt-copper oxide nanosheets for nanoconfined catalytic degradation of contaminants, *Chem. Eng. J.* 449 (2022), 137811, <https://doi.org/10.1016/j.cej.2022.137811>.
- M. Asif, S. Zhang, L. Qiu, Z. Zhang, Ultrahigh permeance functionalised boron nitride membrane for nanoconfined heterogeneous catalysis, *Chem. Catal.* 2 (2022) 1–13, <https://doi.org/10.1016/j.chechat.2022.01.003>.
- D.G. Barceloux, D. Barceloux, Cobalt, *J. Toxicol.: Clin. Toxicol.* 37 (1999) 201–216, <https://doi.org/10.1081/CLT-100102420>.
- P. Shi, R. Su, S. Zhu, M. Zhu, D. Li, S. Xu, Supported cobalt oxide on graphene oxide: highly efficient catalysts for the removal of Orange II from water, *J. Hazard. Mater.* 229–230 (2012) 331–339, <https://doi.org/10.1016/j.jhazmat.2012.06.007>.
- Z. Mao, J. Chen, Y. Yang, D.-J. Wang, L.-J. Bie, B. Fahlman, Novel g-C<sub>3</sub>N<sub>4</sub>/CoO nanocomposites with significantly enhanced visible-light photocatalytic activity for H<sub>2</sub> evolution, *ACS Appl. Mater. Interfaces* 9 (2017), <https://doi.org/10.1021/acsami.7b00370>.
- Y. Ma, B. Ji, X. Lv, D. Xiong, X. Zhao, H. Xie, Z. Zhang, Confined heterogeneous catalysis by boron nitride-Co<sub>3</sub>O<sub>4</sub> nanosheet cluster for peroxymonosulfate oxidation toward ranitidine removal, *Chem. Eng. J.* 435 (2022), 135126, <https://doi.org/10.1016/j.cej.2022.135126>.
- B. Lin, G. Yang, B. Yang, Y. Zhao, Construction of novel three dimensionally ordered macroporous carbon nitride for highly efficient photocatalytic activity, *Appl. Catal. B: Environ.* 198 (2016) 276–285, <https://doi.org/10.1016/j.apcatb.2016.05.069>.
- B. Lin, H. An, X. Yan, T. Zhang, J. Wei, G. Yang, Fish-scale structured g-C<sub>3</sub>N<sub>4</sub> nanosheet with unusual spatial electron transfer property for high-efficiency photocatalytic hydrogen evolution, *Appl. Catal. B: Environ.* 210 (2017) 173–183, <https://doi.org/10.1016/j.apcatb.2017.03.066>.
- D. Vaya, B. Kaushik, P.K. Surolia, Recent advances in graphitic carbon nitride semiconductor: structure, synthesis and applications, *Mater. Sci. Semicond. Process.* 137 (2022), 106181, <https://doi.org/10.1016/j.mssp.2021.106181>.
- G. Lei, Y. Cao, W. Zhao, Z. Dai, L. Shen, Y. Xiao, L. Jiang, Exfoliation of graphitic carbon nitride for enhanced oxidative desulfurization: a facile and general strategy, *ACS Sustain. Chem. Eng.* 7 (2019) 4941–4950, <https://doi.org/10.1021/acssuschemeng.8b05553>.
- Y. Huang, Y. Wang, Y. Bi, J. Jin, M.F. Ehsan, M. Fu, T. He, Preparation of 2D hydroxyl-rich carbon nitride nanosheets for photocatalytic reduction of CO<sub>2</sub>, *RSC Adv.* 5 (2015) 33254–33261, <https://doi.org/10.1039/C5RA04227E>.
- J. Jia, W. Sun, Q. Zhang, X. Zhang, X. Hu, E. Liu, J. Fan, Inter-plane heterojunctions within 2D/2D FeSe<sub>2</sub>/g-C<sub>3</sub>N<sub>4</sub> nanosheet semiconductors for photocatalytic hydrogen generation, *Appl. Catal. B: Environ.* 261 (2020), 118249, <https://doi.org/10.1016/j.apcatb.2019.118249>.
- Y. Wang, L. Li, Y. Wei, J. Xue, H. Chen, L. Ding, J. Caro, H. Wang, Water transport with ultralow friction through partially exfoliated g-C<sub>3</sub>N<sub>4</sub> nanosheet membranes with self-supporting spacers, *Angew. Chem. Int. Ed.* 56 (2017) 8974–8980, <https://doi.org/10.1002/anie.201701288>.
- H. Xu, J. Yan, X. She, L. Xu, J. Xia, Y. Xu, Y. Song, L. Huang, H. Li, Graphene-analogue carbon nitride: novel exfoliation synthesis and its application in photocatalysis and photoelectrochemical selective detection of trace amount of Cu<sup>2+</sup>, *Nanoscale* 6 (2014) 1406–1415, <https://doi.org/10.1039/C3NR04759H>.
- F. Guo, W. Shi, C. Zhu, H. Li, Z. Kang, CoO and g-C<sub>3</sub>N<sub>4</sub> complement each other for highly efficient overall water splitting under visible light, *Appl. Catal. B: Environ.* 226 (2018) 412–420, <https://doi.org/10.1016/j.apcatb.2017.12.064>.
- J. Wang, S. Wang, A critical review on graphitic carbon nitride (g-C<sub>3</sub>N<sub>4</sub>)-based materials: Preparation, modification and environmental application, *Coord. Chem. Rev.* 453 (2022), 214338, <https://doi.org/10.1016/j.ccr.2021.214338>.
- Q. Qin, X. Gao, X. Wu, Y. Liu, NaBH<sub>4</sub>-treated cobalt-doped g-C<sub>3</sub>N<sub>4</sub> for enhanced activation of peroxymonosulfate, *Mater. Lett.* 256 (2019), 126623, <https://doi.org/10.1016/j.matlet.2019.126623>.
- M. Xie, J. Tang, L. Kong, W. Lu, V. Natarajan, F. Zhu, J. Zhan, Cobalt doped g-C<sub>3</sub>N<sub>4</sub> activation of peroxymonosulfate for monochlorophenols degradation, *Chem. Eng. J.* 360 (2019) 1213–1222, <https://doi.org/10.1016/j.cej.2018.10.130>.
- W. Chen, Z. Fan, X. Pan, X. Bao, Effect of confinement in carbon nanotubes on the activity of Fischer–Tropsch iron catalyst, *J. Am. Chem. Soc.* 130 (2008) 9414–9419, <https://doi.org/10.1021/ja800819z>.
- Y. Chen, G. Zhang, H. Liu, J. Qu, Confining free radicals in close vicinity to contaminants enables ultrafast fenton-like processes in the interspacing of MoS<sub>2</sub> membranes, *Angew. Chem. Int. Ed.* 58 (2019) 8134–8138, <https://doi.org/10.1002/anie.201903531>.
- S. Zhang, T. Hedtke, Q. Zhu, M. Sun, S. Weon, Y. Zhao, E. Stavitski, M. Elimelech, J.-H. Kim, Membrane-confined iron oxychloride nanocatalysts for highly efficient heterogeneous fenton water treatment, *Environ. Sci. Technol.* 55 (2021) 9266–9275, <https://doi.org/10.1021/acs.est.1c01391>.
- M.B. Asif, H. Kang, Z. Zhang, Gravity-driven layered double hydroxide nanosheet membrane activated peroxymonosulfate system for micropollutant degradation, *J. Hazard. Mater.* 425 (2022), 127988, <https://doi.org/10.1016/j.jhazmat.2021.127988>.
- X. Liu, L. He, X. Chen, L. Du, X. Gu, S. Wang, M. Fu, F. Dong, H. Huang, Facile synthesis of CeO<sub>2</sub>/g-C<sub>3</sub>N<sub>4</sub> nanocomposites with significantly improved visible-light photocatalytic activity for hydrogen evolution, *Int. J. Hydrog. Energy* 44 (2019) 16154–16163, <https://doi.org/10.1016/j.ijhydene.2019.05.042>.

[31] T.Y. Ma, S. Dai, M. Jaroniec, S.Z. Qiao, Graphitic carbon nitride nanosheet–carbon nanotube three-dimensional porous composites as high-performance oxygen evolution electrocatalysts, *Angew. Chem. Int. Ed.* 53 (2014) 7281–7285, <https://doi.org/10.1002/anie.201403946>.

[32] Y. Zhu, T. Wan, X. Wen, D. Chu, Y. Jiang, Tunable Type I and II heterojunction of CoOx nanoparticles confined in  $g$ - $C_3N_4$  nanotubes for photocatalytic hydrogen production, *Appl. Catal. B: Environ.* 244 (2019) 814–822, <https://doi.org/10.1016/j.apcatb.2018.12.015>.

[33] W. Shi, F. Guo, J. Chen, G. Che, X. Lin, Hydrothermal synthesis of  $InVO_4$ /Graphitic carbon nitride heterojunctions and excellent visible-light-driven photocatalytic performance for rhodamine B, *J. Alloy. Compd.* 612 (2014) 143–148, <https://doi.org/10.1016/j.jallcom.2014.05.207>.

[34] L. Liao, Q. Zhang, Z. Su, Z. Zhao, Y. Wang, Y. Li, X. Lu, D. Wei, G. Feng, Q. Yu, X. Cai, J. Zhao, Z. Ren, H. Fang, F. Robles-Hernandez, S. Baldelli, J. Bao, Efficient solar water-splitting using a nanocrystalline CoO photocatalyst, *Nat. Nanotechnol.* 9 (2014) 69–73, <https://doi.org/10.1038/nnano.2013.272>.

[35] D.K. Mishra, J. Mohapatra, M.K. Sharma, R. Chatterjee, S.K. Singh, S. Varma, S. N. Behera, S.K. Nayak, P. Entel, Carbon doped ZnO: synthesis, characterization and interpretation, *J. Magn. Magn. Mater.* 329 (2013) 146–152, <https://doi.org/10.1016/j.jmmm.2012.09.058>.

[36] S. Wang, Y. Liu, J. Wang, Peroxymonosulfate activation by Fe-Co-O-codoped graphite carbon nitride for degradation of sulfamethoxazole, *Environ. Sci. Technol.* 54 (2020) 10361–10369, <https://doi.org/10.1021/acs.est.0c03256>.

[37] X. Yuan, H. Ge, X. Wang, C. Dong, W. Dong, M.S. Riaz, Z. Xu, J. Zhang, F. Huang, Controlled phase evolution from Co nanochains to CoO nanocubes and their application as OER catalysts, *ACS Energy Lett.* 2 (2017) 1208–1213, <https://doi.org/10.1021/acsenergylett.7b00223>.

[38] Y. Ma, D. Xiong, X. Lv, X. Zhao, C. Meng, H. Xie, Z. Zhang, Rapid and long-lasting acceleration of zero-valent iron nanoparticles@ $Ti_3C_2$ -based MXene/peroxymonosulfate oxidation with bi-active centers toward ranitidine removal, *J. Mater. Chem. A* 9 (2021) 19817–19833, <https://doi.org/10.1039/DITA02046C>.

[39] W. Hayat, Y. Zhang, I. Hussain, X. Du, M. Du, C. Yao, S. Huang, F. Si, Efficient degradation of imidacloprid in water through iron activated sodium persulfate, *Chem. Eng. J.* 370 (2019) 1169–1180, <https://doi.org/10.1016/j.cej.2019.03.261>.

[40] Q. Wang, Y. Shao, N. Gao, W. Chu, X. Shen, X. Lu, J. Chen, Y. Zhu, Degradation kinetics and mechanism of 2,4-Di-tert-butylphenol with UV/persulfate, *Chem. Eng. J.* 304 (2016) 201–208, <https://doi.org/10.1016/j.cej.2016.06.092>.

[41] B. Roshani, N. Karpel vel Leitner, The influence of persulfate addition for the degradation of micropollutants by ionizing radiation, *Chem. Eng. J.* 168 (2011) 784–789, <https://doi.org/10.1016/j.cej.2010.12.023>.

[42] X. Duan, Z. Ao, L. Zhou, H. Sun, G. Wang, S. Wang, Occurrence of radical and nonradical pathways from carbocatalysts for aqueous and nonaqueous catalytic oxidation, *Appl. Catal. B: Environ.* 188 (2016) 98–105, <https://doi.org/10.1016/j.apcatb.2016.01.059>.

[43] Z. Zuo, Z. Cai, Y. Katsumura, N. Chitose, Y. Muroya, Reinvestigation of the acid–base equilibrium of the (bi)carbonate radical and pH dependence of its reactivity with inorganic reactants, *Radiat. Phys. Chem.* 55 (1999) 15–23, [https://doi.org/10.1016/S0969-806X\(98\)00308-9](https://doi.org/10.1016/S0969-806X(98)00308-9).

[44] F. Qi, W. Chu, B. Xu, Modeling the heterogeneous peroxymonosulfate/Co-MCM41 process for the degradation of caffeine and the study of influence of cobalt sources, *Chem. Eng. J.* 235 (2014) 10–18, <https://doi.org/10.1016/j.cej.2013.08.113>.

[45] J. Wang, S. Wang, Effect of inorganic anions on the performance of advanced oxidation processes for degradation of organic contaminants, *Chem. Eng. J.* 411 (2021), 128392, <https://doi.org/10.1016/j.cej.2020.128392>.

[46] Y.-H. Guan, J. Ma, Y.-M. Ren, Y.-L. Liu, J.-Y. Xiao, L. Lin, C. Zhang, Efficient degradation of atrazine by magnetic porous copper ferrite catalyzed peroxymonosulfate oxidation via the formation of hydroxyl and sulfate radicals, *Water Res.* 47 (2013) 5431–5438, <https://doi.org/10.1016/j.watres.2013.06.023>.

[47] C. Zhu, F. Zhu, D.D. Dionysiou, D. Zhou, G. Fang, J. Gao, Contribution of alcohol radicals to contaminant degradation in quenching studies of persulfate activation process, *Water Res.* 139 (2018) 66–73, <https://doi.org/10.1016/j.watres.2018.03.069>.

[48] L. Wang, X. Lan, W. Peng, Z. Wang, Uncertainty and misinterpretation over identification, quantification and transformation of reactive species generated in catalytic oxidation processes: a review, *J. Hazard. Mater.* 408 (2021), 124436, <https://doi.org/10.1016/j.jhazmat.2020.124436>.

[49] H. Xue, A. Meng, T. Yang, Z. Li, C. Chen, Controllable oxygen vacancies and morphology engineering: ultra-high HER/OER activity under base–acid conditions and outstanding antibacterial properties, *J. Energy Chem.* 71 (2022) 639–651, <https://doi.org/10.1016/j.jecchem.2022.04.052>.

[50] J. Lim, Y. Yang, M.R. Hoffmann, Activation of peroxymonosulfate by oxygen vacancies-enriched cobalt-doped black  $TiO_2$  nanotubes for the removal of organic pollutants, *Environ. Sci. Technol.* 53 (2019) 6972–6980, <https://doi.org/10.1021/acs.est.9b01449>.

[51] G.P. Anipsitakis, D.D. Dionysiou, Radical generation by the interaction of transition metals I with common oxidants, *Environ. Sci. Technol.* 38 (2004) 3705–3712, <https://doi.org/10.1012/es0351210>.

[52] W. Tong, Y. Xie, H. Luo, J. Niu, W. Ran, W. Hu, L. Wang, C. Yao, W. Liu, Y. Zhang, Y. Wang, Phosphorus-rich microorganism-enabled synthesis of cobalt phosphide/carbon composite for bisphenol A degradation through activation of peroxymonosulfate, *Chem. Eng. J.* 378 (2019), 122187, <https://doi.org/10.1016/j.cej.2019.122187>.

[53] M. Zhu, J. Miao, X. Duan, D. Guan, Y. Zhong, S. Wang, W. Zhou, Z. Shao, Postsynthesis growth of CoOOH nanostructure on  $SrCo0.6Ti0.4O_3-\delta$  perovskite surface for enhanced degradation of aqueous organic contaminants, *ACS Sustain. Chem. Eng.* 6 (2018) 15737–15748, <https://doi.org/10.1021/acssuschemeng.8b04289>.